Reaction Layer Formation on MgO in the Presence of Humidity

Jacquelyn N. Bracco[1, 2*], Gabriela Camacho Meneses[1], Omar Colón[1], Ke Yuan[3], Joanne E. Stubbs[4], Peter J. Eng[4,5], Anna K. Wanhala[4], Jeffrey D. Einkauf[3], Matthew G. Boebinger[6], Andrew G. Stack[3], Juliane Weber[3]

For submission to ACS Applied Materials and Interfaces

[1]School of Earth and Environmental Sciences, Queens College, City University of New York, Queens, NY, 11367-0904, USA

[2] Earth and Environmental Sciences, Graduate Center, City University of New York, New York, NY, 10016-4309, USA

[3]Chemical Sciences Division, Oak Ridge National Laboratory, Oak Ridge, TN, 37831, USA

[4]Center for Advanced Radiation Sources, The University of Chicago, Chicago, IL, 60637, USA

[5]James Franck Institute, The University of Chicago, Chicago, IL 60637, USA

[6]Center for Nanophase Materials Sciences, Oak Ridge National Laboratory, Oak Ridge, TN, 37831, USA

[*]Corresponding Author: phone: 718-997-3338; email: jacquelyn.bracco@qc.cuny.edu

KEYWORDS

Direct air capture of CO_2, carbon removal, interfacial chemistry, MgO

ABSTRACT

Mineralization by MgO is an attractive potential strategy for direct air capture (DAC) of CO_2 due to its tendency to form carbonate phases upon exposure to water and CO_2. Hydration of MgO during this process is typically assumed to not be rate limiting, even at ambient temperatures. However, surface passivation by hydrated phases likely reduces CO_2 capture capacity. Here, we examine the initial hydration reactions that occur on MgO(100) surfaces to determine if they could potentially impact CO_2 uptake. We first used atomic force microscopy (AFM) to explore changes in reaction layers in water (pH = 6 and 12) and MgO saturated solution (pH = 11) and found the reaction layers on MgO are heterogeneous and non-uniform. To determine how relative humidity (R.H.) affects reactivity, we reacted samples at room temperature in nominally dry N_2 (~11-12% R.H.) for up to 12 hours, humid (>95% R.H.) N_2 for 5, 10, and 15 minutes, and in air at 33% and 75% R.H. for 8 days. X-ray reflectivity and electron microscopy analysis of the samples reveals that hydrated phases form rapidly upon exposure to humid air, but growth of the hydrated reaction layer slows after its initial formation. Reaction layer thickness is strongly correlated with relative humidity, with denser reaction layers forming in 75% R.H. as compared with 33% R.H. or nominally dry N_2. The reaction layers are likely amorphous or poorly crystalline based on grazing incidence x-ray diffraction measurements. After exposure to 75% R.H. in air for 8 days, the reaction layer increases in density as compared to the sample reacted in humid N_2 for 5-15 minutes. This may represent an initial step towards crystallization of the reaction layer. Overall, high relative humidity favors the formation of a hydrated, disordered layer on MgO. Based on our

results DAC in a location with higher relative humidity will be favorable, but growth may slow significantly from initial rates even on short timescales, presumably due to surface passivation.

INTRODUCTION

The latest Intergovernmental Panel on Climate Change Synthesis Report highlights the need for negative emissions strategies, such as direct air capture (DAC) of CO_2 for subsequent storage or utilization, to meet net-zero greenhouse gas emissions targets.[1] Presently, the majority of DAC plants use liquid amines as absorbents for the CO_2,[2] but mineralization is also a potentially promising technique.[3] Mineralization strategies include saline mineralization,[4, 5] conversion of silicate minerals,[6] and weathering of silicate or oxide minerals.[7-11] However, there are challenges associated with mineralization strategies, for example, passivation layers inhibiting CO_2 uptake can form on silicate minerals due to polymerization of silicic acid during dissolution and formation of silica rich leached layers.[7, 12-16] DAC with alkaline metal oxide minerals, such as CaO and MgO, may be cheaper and more feasible compared to other mineral systems if a mineral looping process is used. In this approach, metal carbonates are calcined to form metal oxides that are typically amorphous and highly reactive. These metal oxides react with CO_2 in the atmosphere at ambient conditions for a designated time period to form metal carbonates. They are then calcined again to separate the captured CO_2, which can then be either sequestered in the subsurface,[2, 17] or utilized to make cements[18] or plastics[19], while the MgO or CaO material is reused for further CO_2 capture. Calcining of MgO for CO_2 separation requires lower temperatures (350-600°C[20]) than calcining of CaO (~650-1000°C)[21-23] and therefore may be more cost effective. Industrially, MgO is produced by two main methods: (1) calcination of magnesium-containing minerals,[24] e.g. dolomite or magnesite and (2) from brine or seawater, in which $Mg(OH)_2$ is precipitated which is then calcined. Depending on calcining temperature, the reactivity of the resulting MgO varies.[25]

Currently, the technology readiness level (TRL) for ambient weathering of alkali metal oxides as a strategy for DAC is 4 in a recent cost analysis by Young et al., 2023, which classifies this technology as being in a very early stage of development.[26] In the case of lower TRLs for CO_2 capture technologies, developing accurate estimations of feasibility is crucial as these influence which technologies are chosen for progression and direct approaches (i.e., extrapolation) can underestimate costs.[27] As such, assumptions on rate limiting steps can have an outsized influence on cost estimates. In the analysis of McQueen and coworkers,[17] it is assumed that brucite ($Mg(OH)_2$) forms rapidly and its dissolution rate is rate limiting and the carbonate product is magnesite ($MgCO_3$), rather than amorphous or hydrated carbonate phases. With these assumptions, mineral looping with MgO is expected to be inexpensive (\$46-159/ton of CO_2) and could potentially be used to sequester up to 2-3 Gtons CO_2/year.[17] However, the extent and rate of the reaction of MgO with CO_2 is poorly constrained under conditions relevant for DAC,[28] such as the dependence on temperature and varying relative humidity, which makes it challenging to evaluate how cost effective MgO is for DAC relative to CaO or other techniques.

Recent studies have examined the impact of various parameters on carbonation reactions for DAC during ambient weathering of MgO. For example, a recent study by Rausis et al. demonstrated that under ambient conditions the supply of CO_2 to MgO particles is rate limiting.[28] There is also evidence that hydrated magnesium carbonate phases may passivate $Mg(OH)_2$ surfaces and will thus limit carbonation reaction rates, especially at high temperatures.[29] Growth of amorphous magnesium carbonate occurs even more readily at lower temperatures, such as those used during ambient weathering conditions, causing surface passivation MgO surfaces.[30] At least six different hydrated Mg-carbonate phases with varying water contents are known.[31, 32] Under ambient temperatures and CO_2 partial pressures, precipitation of hydrated magnesium carbonate phases, such as dypingite ($Mg_5(CO_3)_4(OH_2)$~$5H_2O$), is expected but more crucially, Rausis and coworkers were not able to find evidence of magnesite formation.[28] This may be problematic for DAC as hydrated phase formation leads to less CO_2 uptake than would occur if $MgCO_3$ precipitates, based on the crystal volume per CO_2 molecule. Recent work by Weber et al., confirmed hydrated magnesium carbonate phases form on MgO surfaces on samples reacted in air for months to years, with the reaction rate slowing over time due to armoring of the surface by passivation layers.[33] Based on diffusion modeling, the majority of the reaction occurs within the first two years.[33] Rausis et al., had suggested that 90% carbonation of MgO will require 5-27 years, assuming little change in reaction rates over long periods of time.[28] However, Weber and coauthors observed that even after 27 years, 90% carbonation is not reached, suggesting passivation has a significant impact.[33] Knowledge of formation conditions for the hydrated MgO phases is therefore critical for a successful DAC strategy.

While there have been studies on longer term (days to months to years) formation of hydrated carbonate phases,[28, 33] there have been comparatively fewer studies exploring the initial conversion of MgO to $Mg(OH)_2$. For example, while passivation during carbonation appears to pose a challenge, less is known about the impact of the initial hydration reactions on passivation. It is assumed that the first step towards MgO carbonation is hydration of the MgO surface to form $Mg(OH)_2$, followed by subsequent formation of hydrated carbonated mineral phases.[29, 34, 35] The conversion of MgO to $Mg(OH)_2$ in wet environments is thermodynamically favorable and this conversion is known to accelerate under elevated temperatures.[36] Based on near-infrared spectroscopy (NIR) measurements on calcined MgO, $Mg(OH)_2$ forms by conversion of MgO hydroxyl groups into hydrogen bonded groups that form a $Mg(OH)_2$ sheet, which eventually leads to stacking of the $Mg(OH)_2$ sheets.[37] Even at 50°C and 85% R.H., this process occurs quite slow, with x-ray diffraction data only showing evidence for crystalline $Mg(OH)_2$ after 6 hours of reaction.[37] In Rausis et al., they allowed for a two-week period for their MgO to convert to $Mg(OH)_2$ upon addition of saturated water in ambient temperature due to slower reaction rates at lower temperatures.[28] Recent work from Luong and coworkers shows MgO nanocubes transform to disordered $Mg(OH)_2$ nanosheets at ambient temperatures,[30, 38, 39] though the $Mg(OH)_2$ only continues to grow if the relative humidity is greater than 50%.[38] They also showed that while $Mg(OH)_2$ will spontaneously nucleate on MgO in the presence of water films, the reaction can be diffusion limited rather than nucleation limited for larger particles (32 nm wide vs. 8 nm wide).[38] Formation of amorphous magnesium carbonate on these nanocubes in the presence of CO_2 leads to surface passivation by blocking water film access to the MgO particles, which would reduce CO_2 uptake.[30] Overall, these studies highlight the interplay between temperature, relative humidity, and reaction area on hydration behavior at MgO.

While calcined MgO particles used in DAC are more reactive than single-crystal MgO, the reaction mechanisms are expected to be very similar. As such, investigating behavior at more stable crystal faces may provide insights into rate limiting steps for hydration reactions. MgO surfaces are generally hydrophilic,[40] however, recent vibrational sum frequency generation spectra indicate non-H-bond between water and MgO (100) and (111) surfaces which appear to be inconsistent with its hydrophilic nature.[41] Reactions occurring on more stable crystal facets may be more likely to be rate limiting, due to slower reaction kinetics. For example, one of the thermodynamically stable MgO surfaces at ambient conditions is the (100) surface.[42] Previous studies of this surface using ab initio molecular dynamics simulations indicate water will be spontaneously dissociate into H^+ and OH^- groups on the MgO (100) surface where the H^+ will protonate the surface O atoms to form hydroxyl sites.[43] This is similar to the initial step that occurs on calcined MgO.[37] Fourier transform infrared spectroscopy experiments demonstrate water initially reversibly adsorbs at the (100) surface, with water potentially dissociating and forming hydroxyls over longer time periods.[44] In solution, chemical equilibrium favors hydroxylation of the (100) surface and reconstruction of the surface into (111) planes with formation of a $Mg(OH)_2$ layer.[45, 46] These reactions are controlled by the reaction of MgO with H+ ions and thus, the reaction rate decreases at high pH.[47, 48] Correlation of H^+ with the rate of hydroxylation $Mg(OH)_2$ indicates protonation of the surface O on MgO may be an important step leading to dissolution of Mg^{2+} and formation of $Mg(OH)_2$. Availability of water is likely to play a key role in these reactions.

Overall, the steps involved in the reaction are similar for the calcined MgO and (100) MgO, which enables us to utilize single crystal MgO to obtain information on film growth and potential rate limiting steps. Since the initial hydration reaction of MgO occurs fast, even at low temperatures, we utilized single crystal MgO (001) surfaces to study the hydration reactions on the MgO (100) - air interface in the presence of humidity since it can be expected that the reaction at a single crystal surface is slower.[25] Here, we report on measurements resolving how humidity affects the hydroxylation and reaction layer formation on MgO (100) using synchrotron x-ray reflectivity and electron microscopy. We discuss applications to calcined MgO and suggest how this may influence DAC activities.

Methods

Materials

MgO single crystals were grown at ORNL (Oak Ridge National Laboratory) using the carbon arc-fusion technique.[49] Grown MgO crystals were 2-3 cm in size and consisted of high-purity single crystals free of microbubbles. Due to the reactivity of MgO in air, MgO samples were cleaved to expose the (100) surface in a pop-up glove bag or glove box filled with nominally dry N_2 gas. The relative humidity (R.H.) in the bag/box was measured with a handheld meter to be 11-12%. Although this gas was not rigorously free of water vapor, we will hereafter refer to these conditions as "nominally dry". Details of the reaction conditions can be found in Table 1. A subset of samples was reacted in a desiccator in 33% and 75% R.H. air for 8 days (referred to as ex situ samples). The humidity of the desiccator was controlled using saturated NaCl and $MgCl_2$ solutions. The other subset of samples (referred to as in situ samples) was cleaved immediately prior to reacting and transferred to the beamline using a sealed container filled with N_2 at 11-12% R.H.

X-ray Scattering Measurements

Low angle x-ray reflectivity (XRR) measurements were performed at beamline 13-ID-C at the Advanced Photon Source (APS) to determine the thickness, density, and roughness of reaction layers on MgO(100) crystals (lattice parameter = 4.21 Å, unit cell area = 17.72Å^2)[50]. The ex-situ samples were shipped to the APS in bags filled with N_2 gas (< 25% R.H.). At the beamline, the samples were mounted on a 6-circle diffractometer and covered with a Kapton dome under N_2 flow to maintain a controlled environment (~3% R.H.). All measurements for both the ex-situ and in situ samples were collected in flowing, nominally dry N_2 to prevent formation of radicals. At the beamline, one of the samples was exposed to N_2 that was bubbled through water in line (referred to as humid N_2) to expose the sample to a humid environment (>95% R.H.). The sample exposed to humid N_2 was first exposed for 5 minutes, then exposed to nominally dry N_2 for 10 minutes to dry out the gas lines and sample cell, prior to measuring the XRR of the sample. Then the process was repeated twice for 5, 10, and 15 minutes of reaction time with humid N_2. The samples cleaved prior to the measurements were mounted onto the diffractometer within 1-2 hours of cleaving.

Table 1. Reaction conditions and times for the XRR experiments.

Reaction Condition	**Reaction Times**
nominally dry	2 - 12 hours
33%	8 days
75%	8 days
Humid N_2	5, 10, 15 minutes

The setup for the XRR measurements included a Newport kappa six (4 sample + 2 detector) circle diffractometer and a Pilatus 100K pixel array detector (Dectris, Inc.) positioned 1.1 m from the center of rotation. The beam was collimated using two 1 m long, Si mirrors in Kirkpatrick−Baez geometry and the size was defined using slits set to 15 × 500 µm. The longer dimension of the beam cross section was oriented perpendicular to the scattering (horizontal) plane defined by incident and reflected beam vectors. XRR intensity was collected as a function of momentum transfer, $Q = 4\pi \sin(\alpha i)/\lambda$, (where λ is the x-ray wavelength and α_i is the incidence angle with respect to the surface) at a fixed energy (10 keV; λ =1.24 Å). The XRR for the in-situ samples measured in dry or humid N_2 were measured to Q = 0.42 Å^{-1}, which is equivalent to a 2θ of 4.8°. The samples pre-reacted at 33% and 75% R.H. were measured to a 2θ of 6.8°. Grazing incidence x-ray diffraction (GIXRD) scans were collected immediately after collection of the XRR spectra for the 33% and 75% R.H. samples. GIXRD patterns were collected from 2θ = 5 - 64°. Diffracted intensity was measured with the sample surface at a fixed incidence angle of 0.18°, below the critical angle for total external reflection, which enhances surface sensitivity. The center of the detector was fixed at 2° in the horizontal (reflecting) plane and scanned in the vertical plane. A 34 mm x 2.6 mm (horizontal x vertical) region of interest (ROI) was defined such that diffraction features (spots or powder rings) swept through it as the detector 2θ axis was rotated. Raw intensities summed over this ROI are presented with no background subtraction.

Data Fitting

The XRR detector image data were background subtracted and integrated prior to fitting. Models were fit to the XRR data as a function of 2θ in GenX (version 3.6.3).[51, 52] The models included an MgO substrate with varying roughness and one or two thin film layers, of which the density, thickness, and roughness vary, for 4-7 parameters fit per model. Inclusion of additional layers did not substantially improve the quality of the fits and led to non-unique solutions. Fixing the density of one of the thin film layers to that of $Mg(OH)_2$ also did not improve the quality of the fit. Due to the small size of our samples (4-6 mm) in comparison with the beam footprint, we applied a footprint correction in GenX. The full width at half maximum of the gaussian shaped beam was 30 μm (2σ = 12.5 μm). Initial fits used a differential evolution algorithm to minimize χ^2, weighted by the error bars, using the following equation:

$$FOM_{chi2bars} = 1/(N-p) \times \sum i \left((Y_i - S_i)/E_i\right)^2$$

The total number of data points is given by N, p is the number of free parameters in the fit, Y_i is the XRR data, S_i is the model fit, and E_i is the error bars. This method enables a broad search of parameter space while avoiding trapping in local minima. Final fits used the bumps package in GenX to estimate parameter error bars.

In situ Atomic Force Microscopy

In-situ AFM experiments were conducted using a droplet setup using an Asylum Research MFP-3D instrument. MgO crystals were cleaved using a razor blade just before the AFM experiment to expose a fresh mineral surface. PNP-TR-50 AFM tips were used with a resonance frequency of 17 kHz and a force constant of 0.08 N/m. Samples were imaged in contact mode. Applied solutions were unadjusted deionized water (pH = 6), deionized water adjusted using NaOH to pH = 12 and saturated MgO solution with an adjusted pH = 11. MgO saturated solution was prepared by letting powdered, high purity MgO react with deionized water for several weeks. The solution was filtered with a 0.20 μm filter prior to experiments. No effort was made to exclude or remove dissolved gases from air from the solutions.

Focused Ion Beam Preparation

Samples were preserved after the experiments and coated using a conductive carbon layer using a Cressington sputter coater. A Hitachi NB5000 focused ion beam instrument was used to prepare thin foils for TEM characterization after established protocols.[53]

Transmission Electron Microscopy

An FEI Titan (60-300 kV) aberration-corrected scanning/transmission electron microscope (S/TEM) was used for both the transmission electron microscopy (TEM) and scanning transmission electron microscopy (STEM) measurements. STEM electron energy loss spectroscopy (EELS) measurements were carried out using a Gatan Quantum EEL spectrometer with a dispersion level of 0.3 for scans measured on the sample exposed to >95% R.H. and 1 eV/channel for scans measured on the samples pre-reacted with 33% and 75% R.H., respectively. The spectra represent the sums of the areas in the colored rectangles, each pixel of which has a respective EELS spectra. The EELS spectrum images are 2D grids over the area filled with pixels and the respective image is also the annular dark field signal gathered while collecting this data. A JEOL NEOARM TEM was used to acquire STEM energy dispersive x-ray spectroscopy (EDS) maps at 200 kV.

Single Crystal X-ray Diffraction

Diffraction data were collected at 100 K on a Bruker D8 Advance Quest diffractometer with a graphite monochromator using Mo Kα radiation (λ = 0.71073 Å). The frames were integrated with the Bruker SAINT software package using a narrow-frame algorithm. An empirical absorption correction using the multi-scan method SADABS was applied to the data. The structure was solved by direct methods using the Bruker SHELXTL Software Package, version 2018/3. All thermal parameters were refined anisotropically.

Results and Discussion

MgO in Solution

Single crystal XRD analyses confirmed our MgO crystals had crystal chemistry and structure consistent with natural MgO reported in the literature (SI section 1.1, Table S1, S2, Figs. S1, S2). To establish a benchmark for MgO reactivity with water, AFM was used to measure dissolution and secondary phase formation in deionized water (pH not adjusted, pH ~ 6). Post-cleaving and prior to water exposure, samples exhibited characteristic features associated with cleaved MgO surfaces,[46, 54-56] including multilayer cleavage steps arranged parallel to one another (Figs. 1a, S3) and additional steps following a zig-zag pattern (Fig. S4a). Within 20 minutes of exposure, formation of a secondary phase was observed, which continued to grow until 67 minutes of reaction time (Figure S3). This is consistent with previous studies[56] which showed formation of 2-4 nm thick features on the (100) surface of MgO during exposure to ambient air for 6 days.

Since available literature studies report a slower MgO dissolution rate at higher pH,[48] subsequent measurements of secondary phase formation were conducted using deionized water with a pH of 11-12.5, adjusted using NaOH. Secondary phase formation was slower compared to formation in pH 6 water; no significant reaction layer was observed at 30 minutes reaction. Within 57 minutes, formation of surface features was observed, which continued to grow over the total experiment time of 4.5 hours (Fig. 1b, c). Surface features consisted of rounded features of several 10s of nm in size with ~5 nm height based on AFM height image analysis. These are consistent with previous observations by Jordan et al., in deionized water (who used no pH adjustment).[46] To further decrease the reaction rate, MgO-saturated solution with an adjusted pH = 10 was used. Here, surface feature formation was observed within 52 minutes. At a higher pH of 11.5, rounded, platy surface features of several 100s of nm size formed in 1 hour and 20 minutes (Fig. S4). Due to the radius of the AFM tip (~20 nm), rounded features that were observed may be a convolution of the tip morphology and the surface features. Jordan et al., [46] suggests similar features observed in their experiments are (111) MgO nanofacets, possibly a brucite-like layer due to similarities in the (111) MgO and (001) $Mg(OH)_2$ atomic structures.

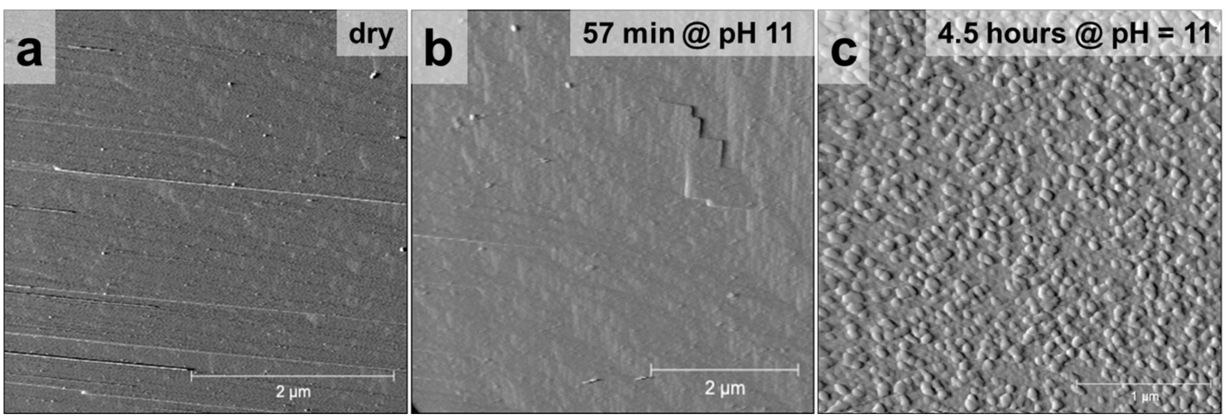

Fig. 1 *In situ AFM images of MgO reacting with deionized water at pH = 12.5. a) Deflection mode AFM image of dry MgO surface immediately after cleaving. b) Deflection mode AFM image of MgO after 57 minutes in solution. c) Deflection mode AFM image of new phase formation after 4.5 h reaction.*

Surface Reactivity in Humid N_2

While the AFM experiments show clear evidence of surface roughening and secondary phase formation in solution, during DAC the MgO will be more likely exposed to air of varying humidity rather than liquid water. Here, we used bright-field (BF) TEM and high-angle annular dark field

(HAADF) STEM imaging to determine reaction layer thickness as a function of relative humidity using line profiles of intensity (Fig. 2). An average reaction layer thickness of ~31.2 ± 0.6 nm was measured for one of the in-situ experiments, which had been reacted in nominally dry N_2 overnight followed by humid N_2 for 3 cycles of 5 minutes exposure each cycle. The reaction layer on the ex-situ sample from the 33% R.H. 8-day experiment was less homogeneous and had a larger range of layer thickness, with an average reaction layer thickness of ~68.9 ± 7.3 nm. For the 75% R.H. 8-day sample, a reaction layer thickness of ~64.0 ± 3.4 nm was measured. A table of individual measurements is given in Table S3.

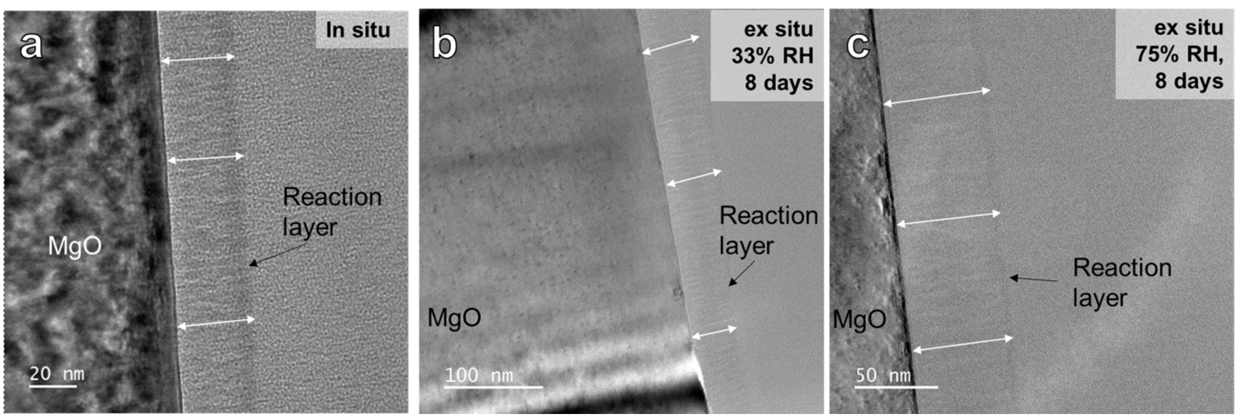

Fig. 2 *Reaction layer thickness measurements using BF-TEM imaging. a) Sample exposed to nominally dry N_2 overnight followed by 3 cycles of 5 minutes exposure to humid N_2, b) ex situ sample exposed to 33% RH for 8 days and c) exposed to 75% RH for 8 days. The left side of each image shows the pristine MgO, the right side is a protective carbon coating, and at the interface, a reaction layer is visible.*

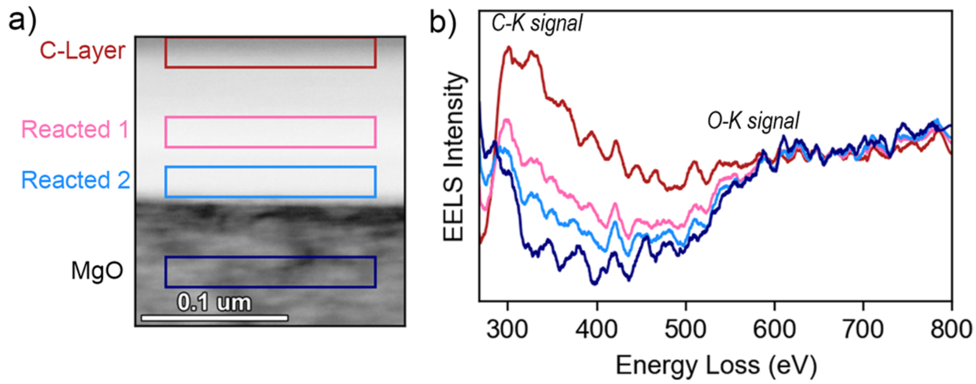

Fig. 3 *STEM-EELS characterization of the sample exposed to 11-12% R.H. N_2 overnight followed by 3 cycles of 5 minutes exposure to humid N_2 (8).* ***(a)*** *STEM Spectrum Image of the region used for EELS with the colored regions across the reaction layer (dark blue = MgO, light blue and pink = reaction layer, red = carbon coating).* ***(b)*** *EELS data that have been background subtracted and summed over the associated regions in (a) showing a large decrease in the carbon signal moving from the protective layer to the reacted layer and no evidence of C in the MgO substrate.*

STEM-EELS was used to acquire spectrum images across the reaction layer from the protective carbon to the unreacted MgO sample (Fig. 3). Different regions (color coded areas marked in Fig. 3a) were selected to compare the carbon signal in the pristine MgO, the reaction layer and the protective carbon layer. Little or no C K-edge signal at 284 eV is observed in the MgO substrate (i.e., no clear peak is observed starting at 284 eV, but a continuous decrease in intensity with increasing energy loss). There is a small quantity of C in the reacted layer immediately adjacent to the MgO and slightly more C is present farther from the interface, at least some of which arises from the carbon coating. However, the oxygen K signal at 532 eV is seen to be consistent in each of the sampled regions indicating the layer contains a similar concentration of oxygen as the pristine material.

When comparing the STEM-EELS characterization of the ex-situ samples reacted at 33% humidity and 75% humidity (Fig. 4), we observe no features attributable to oxygen in the protective carbon layer (yellow in Fig. 4b for 33% R.H., green in Fig. 4e for 75% R.H., corresponding spectra in Fig. 4 c, f), a weak oxygen signal in the reaction layer adjacent to the unreacted MgO surface (orange rectangle in Fig. 4b for 33% R.H., light blue rectangle in Fig. 4e for 75% R.H., corresponding spectra in Fig. 4c, f) and the strongest signal for oxygen in the unreacted MgO substrate (red rectangle in Fig. 4b for 33% R.H., dark blue rectangle in Fig. 4e for 75% R.H., corresponding spectra in Fig. 4c, f). This indicates that the reaction layer contains oxygen, though likely at lower concentration than in the unreacted MgO.

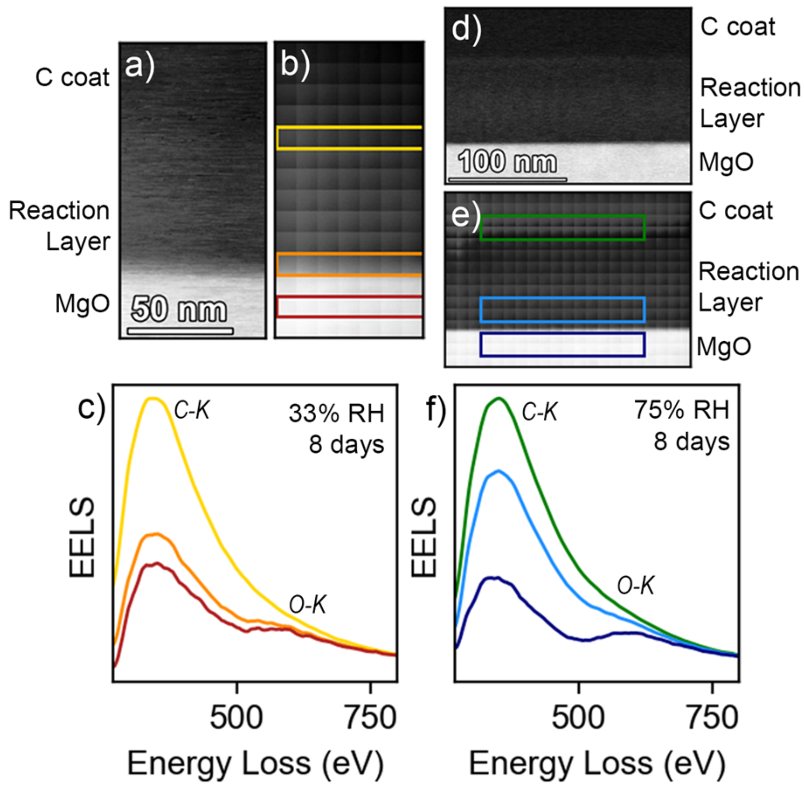

Fig. 4 *Ex situ sample comparison of 33% RH (a-c), 75% RH (d-f). HAADF images are shown in a,d with EELS Spectrum Images seen in b,e. The associated color-coded areas used for the EELS spectra in b, e are shown in c,f.*

To test whether Mg was present in the reaction layer, STEM-EDS maps were made since the Mg EELS edge is located at very high energy. Even though maps are overwhelmed by high Mg signal from bulk MgO, a signal for Mg in the reaction layer was detected (see Fig. S5 in supporting information). The STEM-EELS and STEM-EDS data therefore indicate it is likely that the reaction layer contains Mg and O and to a lesser extent some C. Since hydrogen cannot be reliably detected with either technique, it cannot be clearly determined if the reaction layer might be a hydroxide (e.g., $Mg(OH)_2$) and/or contain minor amounts of a carbonate phase.

Based on the ex-situ TEM and STEM results, we hypothesized that increases in relative humidity and reaction times would increase the thickness and/or coverage of the reaction layer. To measure this more precisely, we used in-situ x-ray reflectivity (XRR). Our first sample was cleaved in a glove bag at 11-12% R.H. and measured under flowing nominally dry N_2. The XRR profile shows a rounded critical angle ~ $2\theta = 0.22°$ followed by a single dip near $2\theta = 2°$ that represents the first minimum in a set of widely spaced thin-films oscillations or Kiessig fringes[57] (Fig. 5a), indicating a thin reaction layer. On a second sample we tested whether the position and magnitude of the oscillation changed over time in the sample cell, but significant changes were not observed even after repeatedly measuring the sample for 12 hours. This suggests that, under relatively dry conditions, the reaction layer that forms on the surface post-cleaving forms rapidly but does not continue to evolve over time. Based on previous data from the literature it is likely there is ~1 monolayer of magnesium hydroxide on the surface and up to 1 monolayer of adsorbed water.[58, 59] The initial reaction layer formation could be due to high energy sites, such as steps or defects, that form in the cleaving process that are more susceptible to initial hydration than terrace sites. Based on the AFM images in Figure 1, there are many steps on cleaved MgO(100) surfaces, which causes the surface to deviate from a mirror flatness. This deviation leads to rounding of the XRR profile at low 2θ, near the critical angle. It is also possible that MgO dust particles that are deposited on the surface during cleaving are also quickly reacting with the limited H_2O in the air. This might be a result since a glove bag was needed to control the relative humidity during cleaving and we were unable to remove any MgO dust or fragments generated during cleaving prior to measurements.

However, rapid adsorption of water on MgO(100) even in relative humidities of less than 0.1% has been previously reported based on ambient pressure x-ray photoelectron spectroscopy (APXPS) and infrared (IR) spectroscopy measurements,[58-60] suggesting that both terrace and step regions will contribute to reaction layer formation.

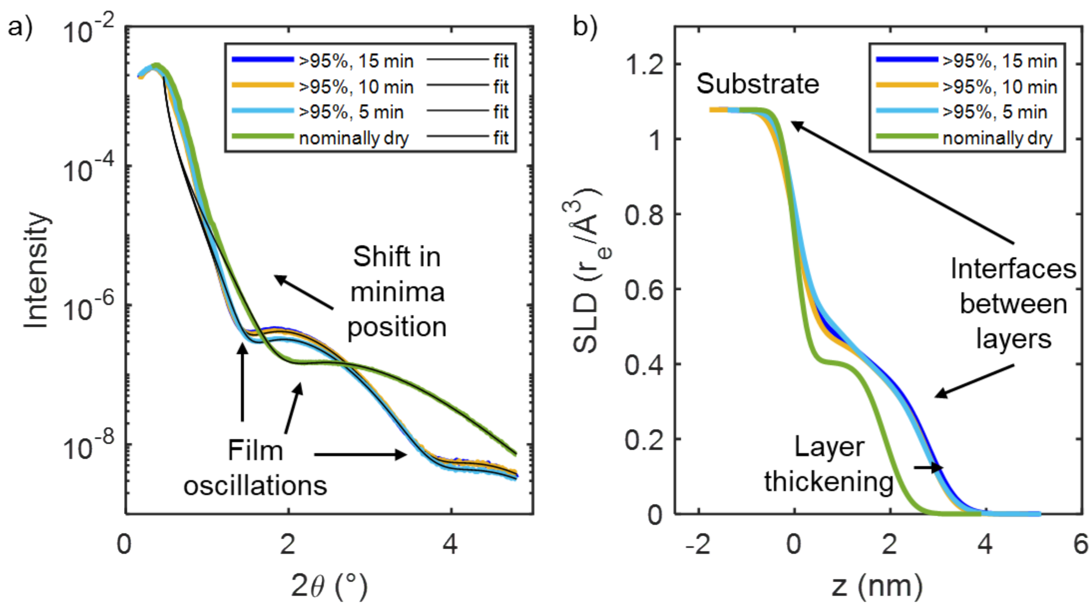

Fig. 5 *XRR profiles (a) for MgO(100) samples reacted as a function of time in humid N_2 and scattering length density (SLD) profiles (b) derived from fits to the data. The critical angle is located at 0.22°.*

To determine if water vapor plays a role in the formation of the hydrated reaction layer, we exposed the sample to humid N_2 for 5, 10, and 15 minutes of exposure time (***Fig. 5***). A reaction layer formed rapidly upon exposure to humid N_2 as evidenced by the shortening of the oscillation period, with two minima now visible in Figure 5a at ~1.4 and 3.9°. The 5-, 10-, and 15-minute XRR spectra appear nearly identical, suggesting the reaction layer thickness and density do not change significantly over this timescale and that the initial reaction layer may be passivating the sample. Based on the scattering length density plot (Fig. 5b), the reaction layer thickens from ~2.5-

3 nm thick to ~4 nm thick, less than that measured by TEM (Fig. 2). However, based on the AFM results (Fig. 1), the MgO surface does not appear to interact uniformly with solution, suggesting reaction layer thickness and coverage may vary across the surface, which may account for the differences in the two measurements. The AFM images have features tens of nm tall on the surface, similar to that measured by TEM. However, the AFM images have features on the surface smaller than 10 nm, which is more similar to the thickness measured from XRR. Based on the XRR fit results (Table 2) for the cleaved sample in nominally dry N_2, the MgO substrate (ρ = 3.58 g/cm^3) had a roughness of 2.31 (±0.02) Å. Parameters were fit for a single film layer with ρ = 1.34 g/cm^3 (±0.01), thickness, d = 18.88 (±0.02) Å, roughness, σ = 4.0 (±0.1) Å) (Fig. 5 b). After 5 minutes of reaction in humid N_2, the MgO substrate had a roughness of 2.8 (±0.1) Å with layer 1 (ρ = 2.05 (±0.05) g/cm^3, d = 10.3 (± 0.6) Å, roughness = 8.3 (±0.6) Å) contact with the substrate, followed by layer 2 (ρ = 1.6 (±0.1) g/cm^3, d = 17.1 (± 0.6) Å, roughness = 4.9 (±0.1) Å) (Fig. 5 b). The XRR data and fit results were similar after 10 and 15 minutes of reaction (Table 1). The scattering length densities (SLD) derived from these fits (Fig. 5b) show evidence of layer thickening and roughness between the layers. For example, z < 0 nm corresponds to the substrate and the curvature near z = 0 indicates there is roughness associated with the substrate. This could be due to steps present on the surface generated during the cleaving process and/or roughening of the surface due to exposure to nominal amounts of humidity. The density of the layer closest to the substrate is less than that of $Mg(OH)_2$, but the density does increase in the humid environment, presumably due to hydroxide formation. Grazing incidence x-ray diffraction measurements were conducted on a separate freshly cleaved sample without reaction with humid nitrogen, but the only measurable diffraction peaks were from the MgO.

Table 2: *Goodness of fits (χ^2), film density (ρ), thickness (d), roughness (σ), and associated standard deviations for the samples.*

R.H., time	Layer 2			Layer 1			Substrate	χ^2
	ρ (g/cm^3)	d (Å)	σ (Å)	ρ (g/cm^3)	d (Å)	σ (Å)	σ (Å)	
dry				1.34 (0.01)	18.88 (0.02)	4.0 (0.1)	2.31 (0.02)	5.7
>95%, 5 min	1.10 (0.04)	17.1 (0.6)	4.9 (0.1)	2.05 (0.05)	10.3 (0.6)	8.3 (0.6)	3.0 (0.1)	4.9
>95%, 10 min	0.94 (0.04)	10.8 (0.5)	4.1 (0.1)	1.57 (0.03)	17.5 (0.6)	6.3 (0.4)	2.27 (0.04)	4.6
>95%, 15 min	0.97 (0.09)	13 (2)	4.6 (0.2)	1.80 (0.1)	14 (2)	9 (1)	2.6 (0.2)	4.9
33%, 8 days				1.94 (0.02)	11.88 (0.03)	0	2.9 (0.1)	5.9
75%, 8 days	0.47 (0.01)	11.15 (0.03)	1.0 (0.1)	2.64 (0.01)	31.31 (0.02)	2.04 (0.02)	4.14 (0.03)	20.5

* *The substrate density was fixed at 3.58 g/cm^3.*

Based on data available in the literature, hydroxylation of MgO may create a stable state.[45, 61, 62] That is, Mg-O bonds are readily hydrolyzed, which breaks the bond. Hydroxide may be able to bind to surface Mg atoms and hydrogens to bind to the O atoms post bond breaking, creating the hydroxyl-terminated surface. We hypothesize that while this occurs quickly in our humid N_2 experiments, as the reaction progresses, there may be fewer available sites for continued reactions over short time periods.

Surface Reactivity as a Function of Relative Humidity

To determine if the sample hydrates under low, medium, and high relative humidity over longer periods of time (8 days), we conducted additional XRR experiments (Fig. 6a). For the sample measured after exposure to 33% R.H. air, there is a single oscillation minimum at $2\theta \sim 2.9°$, which indicates a thin reaction layer. However, the sample measured after exposure to 75% R.H. air showed two oscillation minima, at $2\theta \sim 1.4$ and 3.4°, which indicates the reaction layer is thicker for 75% R.H. than 33% R.H. (Fig. 6a). Models were fit to the data to determine the density, roughness, and thickness of the components of the reaction layer (Table 1). The best fit models for the 33% sample included layer, while the one for the 75% sample included two layers, as evaluated by the weighted χ^2 of the fit (20.5 for a two-layer model for 75% R.H., but 45.7 for a one-layer model). Figure S6 shows a comparison of a fit to the 75% data with 1 layer and 2 layers. For the 33% sample, the MgO substrate had a roughness of 2.9 (± 0.1) Å with a single layer (ρ = 1.94 (± 0.02), d = 11.88 (± 0.03) Å, σ = 0 Å) in contact with the substrate. For the 75% sample, the MgO substrate had a roughness of 4.14 (± 0.03) Å with layer 1 (ρ = 2.64 (± 0.01) g/cm^3, d = 31.31 (± 0.02) Å, σ = 2.04 (± 0.02) Å) (ρ = 0.47 (± 0.01) g/cm^3, d = 11.15 (± 0.03) Å, σ = 1.0 (± 0.1) Å) in contact with the substrate, followed by layer 2 (ρ = 0.47 (± 0.01) g/cm^3, d = 11.15 (± 0.03) Å, σ = 1.0 (± 0.1) Å). The SLD profiles (Fig. 6b) illustrate both the thickening of the reaction layer and the changes in density. For example, the 75% R.H. SLD plot has a greater SLD at z ~ 3 nm than the > 95% R.H., indicating a greater density for the 75% interfacial layer than the >95% R.H. sample. In addition, the SLD profile for the 75% R.H. sample does not drop to 0 until ~5 nm in z, whereas it drops to 0 at ~ 2 nm in z for the 33% R.H. sample. Therefore, over the same period, the reaction layer in the 75% R.H. sample was able to grow more than twice as thick as the 33% R.H. sample (Table 2, Fig. 6b). While the thickness of the reaction layer is about 1 nm thinner for the 5–15 minute exposure to humid N_2 than the 8-day 75% exposure samples, the thickness of the layer closest to the MgO, which is denser than the layer further from the surface, is greater for the 8 days of reaction (~1.5 vs 3.1 nm).

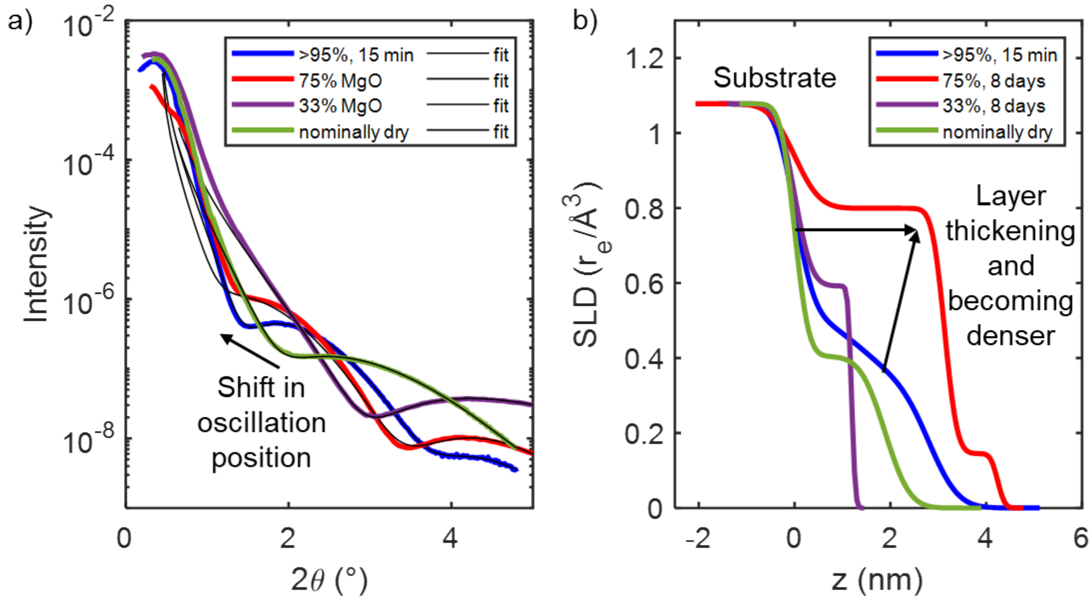

Fig. 6 *(a) X-ray reflectivity profiles and best fits as a function of relative humidities and (b) their associated scattering length density profiles from the XRR data fitting. Due to sample roughness, we were unable to fit the very low Q region ($2\theta < 1$).*

We expected the film that forms on the surface would be brucite, based on previous studies.[38, 39, 63] However, the densities of the layer closest to the substrate for the 75% sample is greater than that of brucite (2.39 g/cm^3). GIXRD was used to determine if crystalline phases were present in the film. The five peaks observed in each of the GIXRD patterns (Fig. 7) are consistent with those expected for periclase, i.e., MgO.[64] There is a broad hump centered around 50° in the pattern for the 33% R.H. sample and potentially the 75% R.H. sample, which may indicate the presence of a nanosized or poorly crystalline material. This position is consistent with one of the brucite peaks (111) at 10 keV[65], which also overlaps with a MgO (periclase) peak (022) at ~49°. However, this is a weak diffraction peak in the brucite powder pattern, though stronger than peaks would be in that region for magnesium carbonate phases including hydromagnesite ($Mg_5(CO_3)_4(OH)_2{\cdot}4H_2O$),[66] nesquehonite ($MgCO_3{\cdot}3H_2O$),[67] and magnesite ($MgCO_3$).[68] We cannot conclusively resolve if the film formed on the surface is a crystalline hydrated phase.

However, there also is no evidence for crystallinity in the BF-TEM images. Further research is needed to conclusively determine if the reaction layer is a crystalline phase or not, but previous studies have observed precipitation of amorphous magnesium hydroxide during reactions between magnesium sulfate and calcium hydroxide[69] as well as precipitation of amorphous phases during reaction of MgO in ambient conditions for time periods shorter than 2 months.[28, 30, 33]

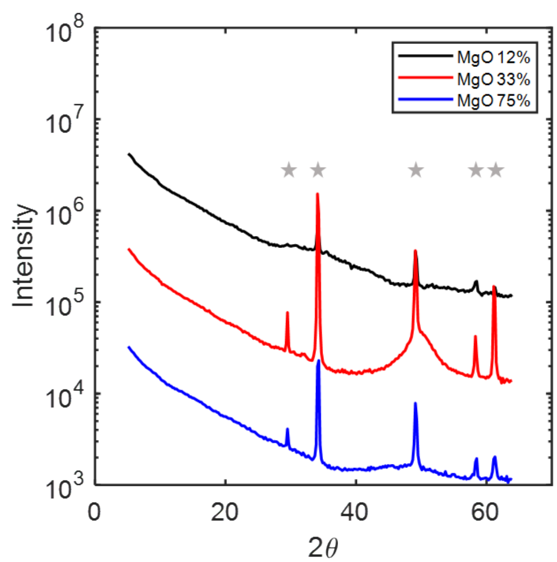

***Fig.** 7 GIXRD measurements from the MgO samples in nominally dry N_2 and after exposure to 33 and 75% R.H. air for 8 days. Stars indicate locations of periclase Bragg peaks, which arise from powder deposited on the surface during cleaving.*

Potential Mechanism for Layer Formation and Implications for Direct Air Capture

Our results demonstrate that reaction layers rapidly form in ambient conditions on MgO(100) surfaces, suggesting that the conversion of MgO hydroxyl groups into hydrogen bonded groups that form an $Mg(OH)_2$ sheet is not rate limiting for ambient temperatures, even in low (~12%) R.H.. Based on the average depth of the reaction layer (~2 nm) we measured from XRR in 12% R.H., stacking of the (likely disordered) $Mg(OH)_2$ sheets also occurs very rapidly. For comparison, a single layer of $Mg(OH)_2$ has a c lattice spacing of 4.766 Å, suggesting there would be about 500 layers of $Mg(OH)_2$ present in a 2 nm reaction layer if the layers were crystalline. We do not observe any evidence of crystallinity in either the TEM measurements or the GIXRD measurements. It is not clear if this lack of crystallinity will inhibit future conversion to carbonate phase. In addition, the reacted layer forms within minutes of exposure to low humidity at ambient temperatures, indicating this initial process is not rate limiting in the context of longer-term weathering of MgO for DAC.

What does appear to be more rate limiting for DAC conditions is the longer term conversion of MgO to $Mg(OH)_2$. As evidenced in our reaction layer thicknesses measured after 5, 10, and 15 minutes of reaction as compared with 8 days, the thickness of the reaction layer changes most appreciably with humidity and less so with reaction time. For example, the 8-day, 75% R.H. reacted sample is only about 25% thicker than the sample reacted for five minutes in humid N_2 despite reacting more than 2000 times as long. Since the hydration of MgO is needed prior to carbonation, the depth to which the hydrated layer can form will also affect the depth of carbonation and may contribute to passivation of the surface. This indicates that sample size is very important to minimize passivation effects. The calcining process also needs to be considered as that can impact particle size and reactivity. For example, when MgO is generated from magnesite ($MgCO_3$) calcination, the calcination temperature determines the resulting MgO reactivity.[25] Slight changes in activation energy for MgO hydration (ranging from 55-75kJ/mol) depending on calcining temperature were observed.[70] The calcining temperature can also cause increases in particle size,[71] which would make it more challenging to access the interior part of the sample. Furthermore, proposed implementation of DAC using MgO uses 1-year looping cycles,[17] however if passivation occurs on very short time scales, shorter looping may be more effective.

In comparison with longer-term studies of 83 – 217 days, while the reacted phases described by Weber et al., are both crystalline and amorphous hydrated Mg-carbonate phases and $Mg(OH)_2$, our measurements have thinner reaction layers with no observable crystallinity. Based on our SLD profiles, changes within the reaction layer over time may lead to increased density within the reaction layer. This was most apparent when comparing the sample reacted in 75% R.H. for 8 days as compared with the sample reacted in humid N_2 for 15 minutes. This implies the changes in density arise from reactions driven by water and its dissociation products, which may be able to continue accessing the reaction layer interface due to the roughness, non-uniformity and/or permeability of the reaction layer observed with XRR and AFM. Since the longer-term reactions of Weber et al. show evidence for crystallinity, the changes in density may be due to the reaction layer restructuring towards a more crystalline phase, presumably through the release of structural water.[72]

Our results show the need for high relative humidity to drive both the initial hydration reactions and to sustain further reactions in the reaction layer. This constrains the optimal reaction conditions for DAC. Since increasing the local relative humidity of air that reacts in DAC is energy intensive, the most energy efficient way would be to have future DAC plants in regions with naturally high relative humidity (e.g., southeast US, etc.). This is in agreement with bench scale studies at 50°C showing that CO_2 capture capacity increases with increasing humidity.[73] In addition, the slow restructuring of the hydroxide layer into a denser and more crystalline phase indicates that the hydration step for DAC is important. In current pilot plants, hydration occurs via spraying of CaO powders directly prior to the CO_2 capture.[74] Our results indicate that the density of the surface layer changes with reaction time and therefore can potentially influence the CO_2 capture potential.

Summary

In conclusion, our results show that MgO reacts rapidly with water, though these initial reaction layers seem to be composed of amorphous or poorly crystalline phases. Based on the TEM results, the alteration layer is not significantly different between the 33% and 75% R.H. sample, though it is thicker than the >95% R.H. sample. However, AFM measurements of MgO in solution suggest the surface may be very patchy post reaction with water. We did not observe any substantial differences in total alteration layer depth as a function of time (5-15 minutes of reaction in humid N_2) but did observe an increase of ~1 nm for the 8 days of reaction in 75% R.H. sample based on the XRR results. In addition, the alteration layer is denser in the sample reacted for 8 days. This suggests that while the initial hydration may be rapid and driven by the presence of water at the surface, additional reactions within the alteration layer can change its structure and/or composition. This may be due to release of structural water if hydrated phases form during the initial reaction. Based on these results, we suggest that reaction times and particle sizes need to be kept as short and small as possible to limit the impacts of passivation by hydration during direct air capture.

AUTHOR INFORMATION

Corresponding Author

* Corresponding Author: phone: 718-997-3338; email: jacquelyn.bracco@qc.cuny.edu

Author Contributions

JNB collected XRR and GIXRD data and analyzed it. GC helped with XRR and GIXRD data analysis. OC helped with XRR and GIXRD data collection. KY helped with XRR and GIXRD data collection and performed ex-situ experiments. JES, PJE and AKW provided beamline support during XRR and GIXRD data collection and aided in data analysis discussion. JE did single crystal XRD measurements. MB helped with TEM characterization and analyzed EELS data. AGS provided part of the funding. JW provided the majority of funding, performed AFM experiments, conducted TEM analysis, and helped collect XRR data. The manuscript was written through contributions of all authors. All authors have given approval to the final version of the manuscript.

Funding Sources

This work was mainly supported by the U.S. Department of Energy, Office of Science, Basic Energy Sciences, Material Sciences and Engineering Division. Part of this research (initial x-ray reflectivity measurements and part of FIB preparation of TEM foils) was funded by an ORNL internal laboratory directed research & development project. Single crystal XRD by JDE was supported by the U.S. Department of Energy, Office of Science, Basic Energy Sciences, Chemical Sciences, Geosciences, and Biosciences Division. XRR and GIXRD measurements were conducted at GeoSoilEnviroCARS (The University of Chicago, Beamline 13-ID-C), Advanced Photon Source (APS), Argonne National Laboratory. GeoSoilEnviroCARS is supported by the National Science Foundation-Earth Sciences (EAR-1634415). J.E.S, A.K.W. and P.J.E. received further support from Department of Energy-GeoScience (DE-SC0019108). This research used resources of the Advanced Photon Source, a U.S. Department of Energy Office of Science User Facility operated for the DOE Office of Science by Argonne National Laboratory under Contract DE-AC02-06CH11357.

Notes

N/A

Supporting Information

single-crystal x-ray diffraction data, unit cell images, additional atomic force microscopy images, measurements of reaction layer thicknesses, additional STEM-EDS images, comparison of x-ray reflectivity fits for one and two species models, .cif file for the single crystal diffraction data

ACKNOWLEDGMENT

This work was mainly supported by the U.S. Department of Energy, Office of Science, Basic Energy Sciences, Materials Sciences and Engineering Division. Part of this research (initial x-ray reflectivity measurements and part of FIB preparation of TEM foils) was funded by an ORNL internal laboratory directed research & development project. TEM characterization was conducted as part of a user project at the Center for Nanophase Materials Sciences (CNMS), which is a US

Department of Energy, Office of Science User Facility at Oak Ridge National Laboratory. We would like to thank James Kolopus for providing the MgO samples used in this study. Jefferey Baxter is acknowledged for FIB sample preparation. Single crystal XRD by JDE was supported by the U.S. Department of Energy, Office of Science, Basic Energy Sciences, Chemical Sciences, Geosciences, and Biosciences Division. XRR and GIXRD measurements were conducted at GeoSoilEnviroCARS (The University of Chicago, Beamline 13-ID-C), Advanced Photon Source (APS), Argonne National Laboratory. GeoSoilEnviroCARS is supported by the National Science Foundation-Earth Sciences (EAR-1634415). J.E.S, A.K.W. and P.J.E. received further support from Department of Energy-GeoScience (DE-SC0019108). This research used resources of the Advanced Photon Source, a U.S. Department of Energy Office of Science User Facility operated for the DOE Office of Science by Argonne National Laboratory under Contract DE-AC02-06CH11357.

ABBREVIATIONS

AFM – atomic force microscopy

APS – advanced photon source

APXPS – ambient pressure x-ray photoelectron spectroscopy

DAC - direct air capture

EDS – energy-dispersive x-ray spectroscopy

GIXRD – grazing incidence x-ray diffraction

IR – infrared spectroscopy

ORNL - Oak Ridge National Laboratory

R.H. – relative humidity

STEM – scanning transmission electron microscopy

STEM-EELS – scanning transmission electron microscopy electron energy loss spectroscopy

HAADF-STEM– high-angle annular dark field scanning transmission electron microscopy

TEM – transmission electron microscopy

BF-TEM – bright-field transmission electron microscopy

XRR – x-ray reflectivity

REFERENCES

(1) IPCC. Ar6 Synthesis Report: Climate Change. In *The Physical Science Basis*, 2021.
(2) McQueen, N.; Gomes, K. V.; McCormick, C.; Blumanthal, K.; Pisciotta, M.; Wilcox, J. A Review of Direct Air Capture (Dac): Scaling up Commercial Technologies and Innovating for the Future. *Progress in Energy* **2021**, *3* (3), 32001-32001.
(3) Fahr, S.; Powell, J.; Favero, A.; Giarrusso, A. J.; Lively, R. P.; Realff, M. J. Assessing the Physical Potential Capacity of Direct Air Capture with Integrated Supply of Low-Carbon Energy Sources. *Greenhouse Gases: Science and Technology* **2022**, *12* (1), 170-188. DOI: https://doi.org/10.1002/ghg.2136.
(4) La Plante, E. C.; Chen, X.; Bustillos, S.; Bouissonnie, A.; Traynor, T.; Jassby, D.; Corsini, L.; Simonetti, D. A.; Sant, G. N. Electrolytic Seawater Mineralization and the Mass Balances That Demonstrate Carbon Dioxide Removal. *ACS ES&T Engineering* **2023**, *3* (7), 955-968. DOI: 10.1021/acsestengg.3c00004.
(5) La Plante, E. C.; Simonetti, D. A.; Wang, J.; Al-Turki, A.; Chen, X.; Jassby, D.; Sant, G. N. Saline Water-Based Mineralization Pathway for Gigatonne-Scale Co2 Management. *ACS Sustainable Chemistry & Engineering* **2021**, *9* (3), 1073-1089. DOI: 10.1021/acssuschemeng.0c08561.
(6) Grayevsky, R.; Reiss, A. G.; Emmanuel, S. Carbon Storage through Rapid Conversion of Forsterite into Solid Oxalate Phases. *Energy & Fuels* **2023**, *37* (1), 509-517. DOI: 10.1021/acs.energyfuels.2c03245.
(7) Miller, Q. R. S.; Schaef, H. T.; Kaszuba, J. P.; Gadikota, G.; McGrail, B. P.; Rosso, K. M. Quantitative Review of Olivine Carbonation Kinetics: Reactivity Trends, Mechanistic Insights, and Research Frontiers. *Environmental Science and Technology Letters* **2019**, *6* (8), 431–442. DOI: 10.1021/acs.estlett.9b00301.
(8) Andreani, M.; Luquot, L.; Gouze, P.; Godard, M.; Hoisé, E.; Gibert, B. Experimental Study of Carbon Sequestration Reactions Controlled by the Percolation of Co2-Rich Brine through Peridotites. *Environmental Science and Technology* **2009**, *43* (4), 1226–1231. DOI: 10.1021/es8018429.
(9) Di Lorenzo, F.; Ruiz-Agudo, C.; Ibañez-Velasco, A.; Gil-San Millán, R.; Navarro, J. A. R.; Ruiz-Agudo, E.; Rodriguez-Navarro, C. The Carbonation of Wollastonite: A Model Reaction to

Test Natural and Biomimetic Catalysts for Enhanced Co2 Sequestration. *Minerals* **2018**, *8* (5), 209. DOI: 10.3390/min8050209.
(10) Kashim, M. Z.; Tsegab, H.; Rahmani, O.; Abu Bakar, Z. A.; Aminpour, S. M. Reaction Mechanism of Wollastonite in Situ Mineral Carbonation for Co2sequestration: Effects of Saline Conditions, Temperature, and Pressure. *ACS Omega* **2020**, *5* (45), 28942–28954. DOI: 10.1021/acsomega.0c02358.
(11) Kelemen, P. B.; McQueen, N.; Wilcox, J.; Renforth, P.; Dipple, G.; Vankeuren, A. P. Engineered Carbon Mineralization in Ultramafic Rocks for Co2 Removal from Air: Review and New Insights. *Chemical Geology* **2020**, *550*, 119628. DOI: 10.1016/j.chemgeo.2020.119628.
(12) Abdolhosseini Qomi, M. J.; Miller, Q. R. S.; Zare, S.; Schaef, H. T.; Kaszuba, J. P.; Rosso, K. M. Molecular-Scale Mechanisms of Co2 Mineralization in Nanoscale Interfacial Water Films. *Nature Reviews Chemistry* **2022**, *6* (9), 598-613. DOI: 10.1038/s41570-022-00418-1.
(13) Kerisit, S. N.; Mergelsberg, S. T.; Thompson, C. J.; White, S. K.; Loring, J. S. Thin Water Films Enable Low-Temperature Magnesite Growth under Conditions Relevant to Geologic Carbon Sequestration. *Environmental Science & Technology* **2021**, *55* (18), 12539-12548. DOI: 10.1021/acs.est.1c03370.
(14) Mergelsberg, S. T.; Rajan, B. P.; Legg, B. A.; Kovarik, L.; Burton, S. D.; Bowers, G. M.; Bowden, M. E.; Qafoku, O.; Thompson, C. J.; Kerisit, S. N.; et al. Nanoscale Mg-Depleted Layers Slow Carbonation of Forsterite (Mg2sio4) When Water Is Limited. *Environmental Science & Technology Letters* **2023**, *10* (1), 98-104. DOI: 10.1021/acs.estlett.2c00866.
(15) Placencia-Gómez, E.; Kerisit, S. N.; Mehta, H. S.; Qafoku, O.; Thompson, C. J.; Graham, T. R.; Ilton, E. S.; Loring, J. S. Critical Water Coverage During Forsterite Carbonation in Thin Water Films: Activating Dissolution and Mass Transport. *Environmental Science & Technology* **2020**, *54* (11), 6888-6899. DOI: 10.1021/acs.est.0c00897.
(16) Nugent, M. A.; Brantley, S. L.; Pantano, C. G.; Maurice, P. A. The Influence of Natural Mineral Coatings on Feldspar Weathering. *Nature* **1998**, *395* (6702), 588-591. DOI: 10.1038/26951.
(17) McQueen, N.; Kelemen, P.; Dipple, G.; Renforth, P.; Wilcox, J. Ambient Weathering of Magnesium Oxide for Co2 Removal from Air. *Nature Communications* **2020**, *11* (1), 3299 DOI: 10.1038/s41467-020-16510-3.
(18) Walling, S. A.; Provis, J. L. Magnesia-Based Cements: A Journey of 150 Years, and Cements for the Future? *Chemical Reviews* **2016**, *116* (7), 4170-4204. DOI: 10.1021/acs.chemrev.5b00463.
(19) Zhang, P.; Chen, K.; Xu, B.; Li, J.; Hu, C.; Yuan, J. S.; Dai, S. Y. Chem-Bio Interface Design for Rapid Conversion of Co₂ to Bioplastics in an Integrated System. *Chem* **2022**, *8* (12), 3363-3381. DOI: 10.1016/j.chempr.2022.09.005 (acccessed 2023/07/10).
(20) Hollingbery, L. A.; Hull, T. R. The Thermal Decomposition of Natural Mixtures of Huntite and Hydromagnesite. *Thermochimica Acta* **2012**, *528*, 45-52. DOI: 10.1016/j.tca.2011.11.002.
(21) Rodriguez-Navarro, C.; Ruiz-Agudo, E.; Luque, A.; Rodriguez-Navarro, A. B.; Ortega-Huertas, M. Thermal Decomposition of Calcite: Mechanisms of Formation and Textural Evolution of Cao Nanocrystals. *American Mineralogist* **2009**, *94* (4), 578-593. DOI: 10.2138/am.2009.3021.
(22) Ćwik, A.; Casanova, I.; Rausis, K.; Koukouzas, N.; Zarębska, K. Carbonation of High-Calcium Fly Ashes and Its Potential for Carbon Dioxide Removal in Coal Fired Power Plants. *Journal of Cleaner Production* **2018**, *202*, 1026-1034. DOI: 10.1016/j.jclepro.2018.08.234.
(23) Grasa, G. S.; Abanades, J. C. Co2 Capture Capacity of Cao in Long Series of Carbonation/Calcination Cycles. *Industrial and Engineering Chemistry Research* **2006**, *45* (26), 8846–8851. DOI: 10.1021/ie0606946.

(24) Strydom, C. A.; van der Merwe, E. M.; Aphane, M. E. The Effect of Calcining Conditions on the Rehydration of Dead Burnt Magnesium Oxide Using Magnesium Acetate as a Hydrating Agent. *Journal of Thermal Analysis and Calorimetry* **2005**, *80* (3), 659-662. DOI: 10.1007/s10973-005-0710-x.
(25) Ruan, S.; Unluer, C. Comparative Life Cycle Assessment of Reactive Mgo and Portland Cement Production. *Journal of Cleaner Production* **2016**, *137*, 258-273. DOI: https://doi.org/10.1016/j.jclepro.2016.07.071.
(26) Young, J.; McQueen, N.; Charalambous, C.; Foteinis, S.; Hawrot, O.; Ojeda, M.; Pilorgé, H.; Andresen, J.; Psarras, P.; Renforth, P.; et al. The Cost of Direct Air Capture and Storage Can Be Reduced Via Strategic Deployment but Is Unlikely to Fall Below Stated Cost Targets. *One Earth* **2023**, *6* (7), 899-917. DOI: https://doi.org/10.1016/j.oneear.2023.06.004.
(27) van der Spek, M.; Ramirez, A.; Faaij, A. Challenges and Uncertainties of Ex Ante Techno-Economic Analysis of Low Trl Co2 Capture Technology: Lessons from a Case Study of an Ngcc with Exhaust Gas Recycle and Electric Swing Adsorption. *Applied Energy* **2017**, *208*, 920-934. DOI: https://doi.org/10.1016/j.apenergy.2017.09.058.
(28) Rausis, K.; Stubbs, A. R.; Power, I. M.; Paulo, C. Rates of Atmospheric Co2 Capture Using Magnesium Oxide Powder. *International Journal of Greenhouse Gas Control* **2022**, *119*, 103701. DOI: 10.1016/j.ijggc.2022.103701.
(29) Zhao, L.; Sang, L.; Chen, J.; Ji, J.; Teng, H. H. Aqueous Carbonation of Natural Brucite: Relevance to Co2 Sequestration. *Environmental Science & Technology* **2010**, *44* (1), 406-411. DOI: 10.1021/es9017656.
(30) Luong, N. T.; Veyret, N.; Boily, J.-F. Co2 Mineralization by Mgo Nanocubes in Nanometric Water Films. *ACS Applied Materials & Interfaces* **2023**, *15* (38), 45055-45063. DOI: 10.1021/acsami.3c10590.
(31) Kurosawa, R.; Takeuchi, M.; Ryu, J. Fourier-Transform Infrared and X-Ray Diffraction Analyses of the Hydration Reaction of Pure Magnesium Oxide and Chemically Modified Magnesium Oxide. *RSC Advances* **2021**, *11* (39), 24292-24311, 10.1039/D1RA04290D. DOI: 10.1039/D1RA04290D.
(32) Santos, H. S.; Nguyen, H.; Venâncio, F.; Ramteke, D.; Zevenhoven, R.; Kinnunen, P. Mechanisms of Mg Carbonates Precipitation and Implications for Co2 Capture and Utilization/Storage. *Inorganic Chemistry Frontiers* **2023**, *10* (9), 2507-2546, 10.1039/D2QI02482A. DOI: 10.1039/D2QI02482A.
(33) Weber, J. S., Vitalii; Yuan, Ke; Anovitz, Lawrence; Ievlev, Anton; Unocic, Raymond; Borisevich, Albina; Boebinger, Matthew; Stack, Andrew. Armoring of Mgo by Passivation Layer Impedes Direct Air Capture of Co2. *Environmental Science and Technology* **2023**, *57* (40), 14929–14937.
(34) Harrison, A. L.; Dipple, G. M.; Power, I. M.; Mayer, K. U. Influence of Surface Passivation and Water Content on Mineral Reactions in Unsaturated Porous Media: Implications for Brucite Carbonation and Co2 Sequestration. *Geochimica et Cosmochimica Acta* **2015**, *148*, 477-495. DOI: 10.1016/j.gca.2014.10.020.
(35) Fricker, K. J.; Park, A.-H. A. Investigation of the Different Carbonate Phases and Their Formation Kinetics During Mg(Oh)2 Slurry Carbonation. *Industrial & Engineering Chemistry Research* **2014**, *53* (47), 18170-18179. DOI: 10.1021/ie503131s.
(36) Kuleci, H.; Schmidt, C.; Rybacki, E.; Petrishcheva, E.; Abart, R. Hydration of Periclase at 350 ∘C to 620 ∘C and 200 Mpa: Experimental Calibration of Reaction Rate. *Mineralogy and Petrology* **2016**, *110* (1), 1-10. DOI: 10.1007/s00710-015-0414-2.

(37) Kondo, A.; Kurosawa, R.; Ryu, J.; Matsuoka, M.; Takeuchi, M. Investigation on the Mechanisms of Mg(Oh)2dehydration and Mgo Hydration by near-Infrared Spectroscopy. *Journal of Physical Chemistry C* **2021**, *125* (20), 10937–10947. DOI: 10.1021/acs.jpcc.1c01470.
(38) Luong, N. T.; Boily, J.-F. Water Film-Driven Brucite Nanosheet Growth and Stacking. *Langmuir* **2023**, *39* (31), 11090-11098. DOI: 10.1021/acs.langmuir.3c01411.
(39) Luong, N. T.; Holmboe, M.; Boily, J.-F. Mgo Nanocube Hydroxylation by Nanometric Water Films. *Nanoscale* **2023**, *15* (24), 10286-10294, 10.1039/D2NR07140A. DOI: 10.1039/D2NR07140A.
(40) Kerisit, S. N.; De Yoreo, J. J. Effect of Hydrophilicity and Interfacial Water Structure on Particle Attachment. *The Journal of Physical Chemistry C* **2020**, *124* (9), 5480-5488. DOI: 10.1021/acs.jpcc.9b12053.
(41) Adhikari, N. M.; Tuladhar, A.; Wang, Z.; De Yoreo, J. J.; Rosso, K. M. No Hydrogen Bonding between Water and Hydrophilic Single Crystal Mgo Surfaces? *The Journal of Physical Chemistry C* **2021**, *125* (47), 26132-26138. DOI: 10.1021/acs.jpcc.1c06486.
(42) Geysermans, P.; Finocchi, F.; Goniakowski, J.; Hacquart, R.; Jupille, J. Combination of (100), (110) and (111) Facets in Mgo Crystals Shapes from Dry to Wet Environment. *Physical Chemistry Chemical Physics* **2009**, *11* (13), 2228-2233, 10.1039/B812376D. DOI: 10.1039/B812376D.
(43) Ding, Z.; Selloni, A. Hydration Structure of Flat and Stepped Mgo Surfaces. *Journal of Chemical Physics* **2021**, *154* (11), 114708. DOI: 10.1063/5.0044700.
(44) Foster, M.; Furse, M.; Passno, D. An Ftir Study of Water Thin Films on Magnesium Oxide. *Surface Science* **2002**, *502-503*, 102-108. DOI: https://doi.org/10.1016/S0039-6028(01)01906-9.
(45) Mejias, J. A.; Berry, A. J.; Refson, K.; Fraser, D. G. The Kinetics and Mechanism of Mgo Dissolution. *Chemical Physics Letters* **1999**, *314* (5-6), 558-563. DOI: 10.1016/S0009-2614(99)00909-4.
(46) Jordan, G.; Higgins, S. R.; Eggleston, C. M. Dissolution of the Periclase (001) Surface: A Scanning Force Microscope Study. *American Mineralogist* **1999**, *84* (1-2), 144-151. DOI: 10.2138/am-1999-1-216.
(47) Baumann, S. O.; Schneider, J.; Sternig, A.; Thomele, D.; Stankic, S.; Berger, T.; Grönbeck, H.; Diwald, O. Size Effects in Mgo Cube Dissolution. *Langmuir* **2015**, *31* (9), 2770-2776. DOI: 10.1021/la504651v.
(48) Fedoročková, A.; Raschman, P. Effects of Ph and Acid Anions on the Dissolution Kinetics of Mgo. *Chemical Engineering Journal* **2008**, *143* (1), 265-272. DOI: https://doi.org/10.1016/j.cej.2008.04.029.
(49) Abraham, M. M.; Butler, C. T.; Chen, Y. Growth of High-Purity and Doped Alkaline Earth Oxides: I. Mgo and Cao. *The Journal of Chemical Physics* **2003**, *55* (8), 3752-3756. DOI: 10.1063/1.1676658 (acccessed 7/10/2023).
(50) Hazen, R. M. Effects of Temperature and Pressure on the Cell Dimension and X-Ray Temperature Factors of Periclase. *American Mineralogist* **1976**, *61* (3-4), 266-271. (acccessed 7/10/2023).
(51) Bjorck, M.; Andersson, G. Genx: An Extensible X-Ray Reflectivity Refinement Program Utilizing Differential Evolution. *Journal of Applied Crystallography* **2007**, *40* (6), 1174-1178. DOI: doi:10.1107/S0021889807045086.
(52) Glavic, A.; Bjorck, M. Genx 3: The Latest Generation of an Established Tool. *Journal of Applied Crystallography* **2022**, *55* (4), 1063-1071. DOI: doi:10.1107/S1600576722006653.
(53) Mayer, J.; Giannuzzi, L. A.; Kamino, T.; Michael, J. Tem Sample Preparation and Fib-Induced Damage. *MRS Bulletin* **2007**, *32* (5), 400-407. DOI: 10.1557/mrs2007.63.

(54) Abriou, D.; Creuzet, F.; Jupille, J. Characterization of Cleaved Mgo(100) Surfaces. *Surface Science* **1996**, *352-354*. DOI: 10.1016/0039-6028(95)01187-0.
(55) Abriou, D.; Jupille, J. Self-Inhibition of Water Dissociation on Magnesium Oxide Surfaces. *Surface Science* **1999**, *430* (1), L527-L532. DOI: 10.1016/S0039-6028(99)00410-0.
(56) Krueger, B. J.; Ross, J. L.; Grassian, V. H. Formation of Microcrystals, Micropuddles, and Other Spatial Inhomogenieties in Surface Reactions under Ambient Conditions: An Atomic Force Microscopy Study of Water and Nitric Acid Adsorption on Mgo(100) and Caco 3(1014). *Langmuir* **2005**, *21* (19), 8793-8801. DOI: 10.1021/la051378j.
(57) Als-Nielsen, J.; McMorrow, D. Refraction and Reflection from Interfaces. In *Elements of Modern X-Ray Physics*, 2011; pp 69-112.
(58) Newberg, J. T.; Starr, D. E.; Yamamoto, S.; Kaya, S.; Kendelewicz, T.; Mysak, E. R.; Porsgaard, S.; Salmeron, M. B.; Brown, G. E.; Nilsson, A.; Bluhm, H. Autocatalytic Surface Hydroxylation of Mgo(100) Terrace Sites Observed under Ambient Conditions. *Journal of Physical Chemistry C* **2011**, *115* (26), 12864–12872. DOI: 10.1021/jp200235v.
(59) Newberg, J. T.; Starr, D. E.; Yamamoto, S.; Kaya, S.; Kendelewicz, T.; Mysak, E. R.; Porsgaard, S.; Salmeron, M. B.; Brown, G. E.; Nilsson, A.; Bluhm, H. Formation of Hydroxyl and Water Layers on Mgo Films Studied with Ambient Pressure Xps. *Surface Science* **2011**, *605* (1-2), 89-94. DOI: 10.1016/j.susc.2010.10.004.
(60) Björneholm, O.; Hansen, M. H.; Hodgson, A.; Liu, L. M.; Limmer, D. T.; Michaelides, A.; Pedevilla, P.; Rossmeisl, J.; Shen, H.; Tocci, G.; et al. Water at Interfaces. In *Chemical Reviews*, 2016; Vol. 116, pp 7698-7726.
(61) Carrasco, E.; Brown, M. A.; Sterrer, M.; Freund, H. J.; Kwapien, K.; Sierka, M.; Sauer, J. Thickness-Dependent Hydroxylation of Mgo(001) Thin Films. *Journal of Physical Chemistry C* **2010**, *114* (42), 18207–18214. DOI: 10.1021/jp105294e.
(62) Ončák, M.; Włodarczyk, R.; Sauer, J. Water on the Mgo(001) Surface: Surface Reconstruction and Ion Solvation. *Journal of Physical Chemistry Letters* **2015**, *6* (12), 2310–2314. DOI: 10.1021/acs.jpclett.5b00885.
(63) Lee, J. H.; Eun, J. H.; Kim, S. G.; Park, S. Y.; Lee, M. J.; Kim, H. J. Hydration Behavior of Mgo Single Crystals and Thin Films. *Journal of Materials Research* **2003**, *18* (12), 2895–2903. DOI: 10.1557/JMR.2003.0404.
(64) Howard, E. S. Circular of the Bureau of Standards No. 539 Volume 1::Standard X-Ray Diffraction Powder Patterns. , National Institute of Standards and Technology, Gaithersburg, MD: 1953.
(65) Catti, M.; Ferraris, G.; Hull, S.; Pavese, A. Static Compression and H Disorder in Brucite, Mg(Oh)2, to 11 Gpa: A Powder Neutron Diffraction Study. *Physics and Chemistry of Minerals* **1995**, *22* (3), 200-206. DOI: 10.1007/BF00202300.
(66) Akao, M.; Iwai, S. The Hydrogen Bonding of Hydromagnesite. *Acta Crystallographica Section B* **1977**, *33* (4), 1273-1275. DOI: doi:10.1107/S0567740877005834.
(67) Stephan, G. W.; MacGillavry, C. H. The Crystal Structure of Nesquehonite, Mgco3.3h2o. *Acta Crystallographica Section B* **1972**, *28* (4), 1031-1033. DOI: doi:10.1107/S0567740872003668.
(68) Markgraf, S. A.; Reeder, R. J. High-Temperature Structure Refinements of Calcite and Magnesite. *American Mineralogist* **1985**, *70* (5-6), 590-600. (acccessed 8/7/2023).
(69) Ziegenheim, S.; Szabados, M.; Kónya, Z.; Kukovecz, Á.; Pálinkó, I.; Sipos, P. Differential Precipitation of Mg(Oh)2 from Caso4·2h2o Using Citrate as Inhibitor-a Promising Concept for

Reagent Recovery from Mgso4 Waste Streams. *Molecules (Basel, Switzerland)* **2020**, *25* (21), 5012. DOI: 10.3390/molecules25215012.
(70) Thomas, J. J.; Musso, S.; Prestini, I. Kinetics and Activation Energy of Magnesium Oxide Hydration. *Journal of the American Ceramic Society* **2014**, *97* (1), 275-282. DOI: 10.1111/jace.12661.
(71) Huang, L.; Yang, Z.; Wang, S. Influence of Calcination Temperature on the Structure and Hydration of Mgo. *Construction and Building Materials* **2020**, *262*, 120776. DOI: 10.1016/j.conbuildmat.2020.120776.
(72) Schaef, H. T.; Windisch, C. F.; McGrail, B. P.; Martin, P. F.; Rosso, K. M. Brucite [Mg(Oh2)] Carbonation in Wet Supercritical Co2: An in Situ High Pressure X-Ray Diffraction Study. *Geochimica et Cosmochimica Acta* **2011**, *75* (23), 7458-7471. DOI: 10.1016/j.gca.2011.09.029.
(73) Ding, Y.-D.; Song, G.; Liao, Q.; Zhu, X.; Chen, R. Bench Scale Study of Co2 Adsorption Performance of Mgo in the Presence of Water Vapor. *Energy* **2016**, *112*, 101-110. DOI: https://doi.org/10.1016/j.energy.2016.06.064.
(74) Plumer, B. In a U.S. First, a Commercial Plant Starts Pulling Carbon from the Air. *New York Times*, 2023. https://www.nytimes.com/2023/11/09/climate/direct-air-capture-carbon.html.

Table of Content Graphic